The Journal of Chemical Physics ARTICLE pubs.aip.org/aip/jcp

Probing symmetry-driven DEA dynamics in ozone investigated by velocity slice imaging technique

Cite as: J. Chem. Phys. 165, 134307 (2026); doi: 10.1063/5.0350118
Submitted: 28 June 2026 • Accepted: 12 September 2026 •
Published Online: 1 October 2026

View Online Export Citation CrossMark

Melvin Varghese,[1] Dharun J,[1] Nigel J. Mason,[2] E. Krishnakumar,[3] Vaibhav S. Prabhudesai,[4,a)] and Krishnendu Gope[1,a)]

AFFILIATIONS

[1] Indian Institute of Science Education and Research, Thiruvananthapuram 695551, India
[2] University of Kent, Canterbury CT2 7NH, United Kingdom
[3] Raman Research Institute, Bengaluru 560080, India
[4] Tata Institute of Fundamental Research, Mumbai 400005, India

Note: This paper is part of the 2026 JCP Emerging Investigators Special Collection.
[a)] **Authors to whom correspondence should be addressed:** vaibhav@tifr.res.in and krishnendu.gope@iisertvm.ac.in

ABSTRACT

We report the results of a comprehensive experimental investigation of dissociative electron attachment (DEA) to ozone using the velocity slice imaging technique. We reveal several channels that yield both O^- and O_2^- from negative-ion resonances formed by electron attachment. Our results demonstrate that DEA to ozone proceeds through competition between symmetric and asymmetric dissociation pathways. This is governed by excitation of symmetric, asymmetric, and bending vibrational modes and likely involves vibronic coupling between the symmetry of the negative ion resonance states. At 1.6 eV, symmetric dissociation results in vibrationally excited O_2 and O_2^- with near-thermal kinetic energies. An additional asymmetric dissociation pathway driven by overlapping contributions from $^2A_1$ and $^2B_2$ states producing rotationally excited O_2 with enhanced translational energy is identified. DEA from the second resonance yields both O^- and O_2^- with considerable internal energies arising from a single anionic state ($^2B_2$) proceeding via an asymmetric dissociation mechanism. In the 4.1 – 4.4 eV region, overlapping resonances with A_1 and B_2 symmetry lead to asymmetric dissociation, accompanied by a notable increase in internal excitations of the molecular moieties. This also provides experimental evidence for the previously proposed $^2A_1$ shape resonance at 4.2 eV. At higher energies around 6.9 eV, angular distribution analysis reveals a contribution from an additional $^2A_1$ state, in contrast to the theoretically predicted $^2B_2$ state. These findings establish a unified picture of competing symmetric and asymmetric dissociation mechanisms that produce highly internally excited and chemically reactive fragments.

Published under an exclusive license by AIP Publishing. https://doi.org/10.1063/5.0350118

12 October 2026 11:14:18

INTRODUCTION

Understanding the dissociation dynamics of electronically excited polyatomic molecules is of fundamental interest in chemical physics and provides insight into non-adiabatic vibronic coupling.[1–5] Such coupling governs how excess energy in electronic degrees of freedom is redistributed among different vibrational modes, thereby controlling the internal excitation of the products and kinetic energy release of the reaction.[6] These internally excited species, which often initiate further reactions, are important in understanding the formation and decay of large complex molecules in various environments such as the interstellar medium, planetary atmospheres, and industrial plasmas.[7–16]

Molecules with C_{2v} symmetry, such as the XO_2 (OXO) systems (where X = O, S, N, Cl, etc.), have structural features that enable complex dissociation dynamics,[17–19] leading to the formation of rovibrationally excited species that are highly reactive.[20–23] The energy redistribution into three vibrational modes, namely symmetric stretch, asymmetric stretch, and bending, of the excited electronic state dictates dissociation pathways. These pathways yield fragments with distinct rovibrational energy distributions and, consequently, different chemical reactivities. In the two-body breakup of these molecules, dissociation is termed symmetric if the central atom (X) separates while the two terminal oxygen atoms combine to form an O_2 fragment. This pathway is typically associated with excitation of the symmetric stretching and bending modes and produces

Published under an exclusive license by AIP Publishing

vibrationally excited O_2 with relatively low kinetic energy (KE).[17,24,25] This was first reported by Miller *et al.* in their explanation of the experimental observations of highly vibrationally excited O_2 from the photodissociation of ozone.[26] In contrast, asymmetric dissociation is associated with dominant asymmetric vibrations that impart an impulse along the dissociating bond, resulting in rotationally excited XO fragments with distinct internal energy distributions.[17,18] Understanding the competition between these mechanisms is crucial, as high internal excitations drive reactions that are otherwise inaccessible.[20–23]

Ozone (O_3), a prototypical molecule with C_{2v} symmetry, plays a critical role in Earth's atmosphere. In the stratosphere, it forms a protective layer that absorbs nearly all harmful UV-B radiation from the Sun, while also acting as the most important greenhouse gas after CO_2 and CH_4.[27,28] In the troposphere, O_3 photolysis initiates oxidation of pollutants such as carbon monoxide and methane, thereby regulating their atmospheric lifetimes and transforming them into less harmful species.[29] Furthermore, it acts as a strong oxidant and is formed as a secondary pollutant via photochemical reactions between volatile organic compounds and nitrogen oxides in the troposphere.[29] Ever since the discovery of ozone holes over Antarctica during the Arctic winter, O_3 has been the subject of considerable experimental investigations using UV absorption spectroscopy to study electronic transitions,[30–32] laser-induced fluorescence,[33–35] and cavity ring-down[36,37] techniques to measure lifetimes and photodissociation quantum yields. Crossed molecular beam experiments have probed state-resolved reaction dynamics with atoms and small radicals.[38–40] Electron scattering experiments on O_3 include elastic and inelastic scattering measurements, electron-energy loss spectra, and electron-impact ionization to determine cross sections and excitation thresholds.[41–47] Complementary ion-beam collision studies have investigated associative detachment and three-body attachment mechanisms by directing O^- and O_2^- beams at O_3 target.[48,49] The mass-spectrometric study of ozone by Curran reported a very weak O_3^- signal, in addition to O^- and O_2^-, indicating a metastable bound ozone anion under electron impact.[50] Allan *et al.* later demonstrated that O_3^- formation is strongly enhanced at higher sample pressures and arises via three-body attachment or ion–molecule reactions.[51] Matejcik and co-workers subsequently confirmed that low-energy electron attachment to oxygen/ozone clusters efficiently produces intact cluster anions along with O_3^-, showing that dense gas and cluster environments are the natural regime where this otherwise very weak ion becomes observable.[47]

In particular, low-energy electron collisions with O_3 have attracted significant interest[24,42,44,52–55] over recent decades as researchers seek to explore the chemical pathways responsible for stratospheric O_3 depletion[56] and the Antarctic ozone hole.[57] Cosmic ray ionization of atmospheric gases such as O_2 and N_2 generates a flux of low-energy electrons in the polar stratosphere,[58] with additional contributions from solar photoionization of low ionisation potential atmospheric constituents, such as halogenated compounds and organic precursors.[59] These low-energy secondary electrons can cause dissociative electron attachment (DEA) to O_3, promoting fragmentation pathways that contribute to enhanced O_3 depletion.[58,60]

Early DEA investigations have identified several principal negative-ion resonances in O_3: a dominant feature near 1.4 eV producing O^-, an endothermic channel to O_2^- peaking near 1.2 eV, and broader resonances around ~3 and ~7.5 eV that involve more complex dissociation pathways.[24,45,50,51,53,61–63] Rangwala *et al.*[53] reported absolute cross sections for O^- and O_2^- as a function of incoming electron energy. These values near the first peak were reported to be $\sim 3.7 \times 10^{-17}$ cm^2 for O^- at 1.4 eV and $\sim 1.7 \times 10^{-17}$ cm^2 at 1.2 eV for O_2^-. The O_2^- cross section was further corrected by Cicman *et al.*[64] to $\sim 2.3 \times 10^{-17}$ cm^2, peaking at 1 eV. Furthermore, Allan *et al.*[52] have reported the production of vibrationally excited O_2^- from DEA to ozone around 1.2 – 2 eV, where O_2^- ($v \geq 4$) was formed with a cross section $\sim 2.7 \times 10^{-17}$ cm^2 at 1.7 eV, undergoing autodetachment. Allan *et al.*[52] identified two shape resonances, A_1 at ~4.2 eV that contributes to the DEA at 3.2 eV and B_2 at ~6.6 eV, arising from the capture of the incident electron into the σ^* orbitals, which are strongly antibonding along the O – O bonds. Both resonances excite vibrational modes, with excitation of the asymmetric stretch mediated by non-adiabatic vibronic coupling between the A_1 and B_2 states.[5,51] A low-energy feature around 1.3 eV was attributed to a core-excited resonance and is characterized by minimal Kinetic Energy Release (KER), whereas the prominent peak near 3.2 eV, which exhibited significantly larger KER, was assigned to an A_1 shape resonance. Angular distributions of O^- corresponding to the ~3.2 eV resonance have also been reported for limited angles (0° – 140°).[51] Based on the ion KE analysis, Walker *et al.* suggested that both the O^- and O_2^- channels around this energy originate from a single anionic resonance state, with dissociation proceeding along the asymmetric stretch coordinate.[24] Allan *et al.* also noted that the 7.5 eV peak observed in the O^- channel of DEA is a Feshbach resonance.[51]

Theoretical studies using *ab initio* static potentials, R-matrix, and Schwinger multichannel methods have predicted shape and core-excited resonances, particularly in the $^2A_1$ and $^2B_2$ symmetry channels whose energies and resonance widths govern vibrational excitation and DEA pathways.[5,55,65–69] Previous investigations have identified the primary resonance regions in O_3^- and estimated the translational energy partitioning among the fragments. However, determining the fragment angular distributions at all angles is necessary to validate the symmetries of the underlying resonant states and to achieve a comprehensive understanding of dissociation dynamics across all DEA resonances, which remain largely unexplored. As a result, the nature of these Negative Ion Resonant States (NIRS) remains poorly understood, despite their critical importance in atmospheric chemistry and plasma environments.

The Velocity Slice Imaging (VSI) technique may be used as a highly sensitive probe of the dissociation dynamics of DEA and, hence, of the short-lived NIRS and their associated potential energy landscapes. Accordingly, in this study, we investigate DEA to O_3 using the VSI technique to obtain both energy- and angle-resolved momentum images of O^- and O_2^- fragment ions. Particular emphasis is placed on the identification of the symmetries of resonant states by analyzing the angular distributions extracted from the measured momentum images.

Experimental methods

The experiments were carried out using a VSI setup, as described elsewhere.[17,18,70–72] Here, we provide a short description of the setup. An effusive molecular beam, generated through a

12 October 2026 11:14:18

Published under an exclusive license by AIP Publishing

capillary, intersects at right angles with a magnetically collimated pulsed electron beam (pulse width of 200 ns). The molecular beam is aligned along the axis of the time-of-flight mass spectrometer, which also acts as a VSI spectrometer when appropriate potentials are applied to various electrodes. The spectrometer consists of a single-element electrostatic lens and a flight tube. Ion detection is achieved using a 2-D position-sensitive detector (PSD) composed of three 75 mm microchannel plates in a Z-stack configuration, followed by a phosphor screen. Ions generated in the interaction region are extracted by a pulsed electric field, applied 100 ns after the electron beam pulse. The electron beam pulse is produced by a thermionic-emission gun with an energy resolution of 0.5 eV.

The ions produced are velocity-focused onto the 2-D PSD by optimizing the electrode voltages. The detector is activated for a 100 ns window by applying an 80 ns-wide 2 kV pulsed bias. A central slice of the Newton sphere is recorded by temporally synchronizing the 2 kV detector pulse with the extraction pulse. The resulting phosphor screen images are captured with a CCD camera. We performed the image calibration by obtaining the O^- images from DEA to O_2. The images were obtained at three different electron energies around the resonance peak at 6.5 eV. The known KE of the fragments was used to calibrate the pixel positions to the ions' initial momenta. Using this calibration, the pixel images were converted into momentum images, thereby enabling determination of the KE and angular distributions of the anionic fragments. Sufficient purity (~28%) samples of O_3 were prepared and purified on-site at the Open University (UK) facility for these measurements, as they readily decompose under UV exposure or upon contact with metal surfaces. The detailed methodology of preparation and purification of O_3 is described in the supplementary material, Section S1.

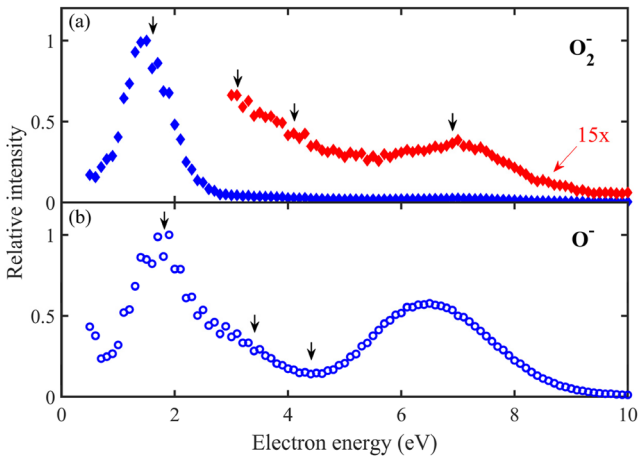


FIG. 1. (a) O_2^- and (b) O^- ion yield as a function of incident electron energy. In the 3 – 10 eV range, the O_2^- signal has been magnified by a factor of 15 to enhance visibility (shown in red). The black arrows indicate the electron energies at which velocity slice images were recorded and presented.

RESULTS AND DISCUSSIONS

DEA to O_3 leads to the formation of O_2^- + O and O^- + O_2 fragmentation channels. The experimentally obtained ion-yield curves for these channels are presented in Fig. 1. Previous DEA investigations have identified distinct O_2^- ion peaks at 1.2, 3, and 7.3 eV, and O^- ion peaks near 1.4, 3, and 7.5 eV.[53,63] The present measurements are in agreement with these reported values, except for the O^- third peak expected at 7.5 eV. The dominant impurity in the molecular beam is O_2, originating from the rapid dissociation of O_3 upon contact with metal surfaces.[73,74] This O_2 impurity gives rise to a strong O^- peak at 6.5 eV,[75] masking the O^- signal from O_3 expected at 7.5 eV. Furthermore, the 3 eV feature of O^- appears as a shoulder rather than a distinct peak, which is attributed to the overlap from the trailing edge of the preceding intense peak at 1.3 eV. This overlap arises from the intrinsic finite energy spread of 0.5 eV of the incident electron beam. The following sections present a detailed investigation of the DEA dynamics near the first two peaks in O^- channel and three peaks in O_2^- channel as indicated by the black arrows in Fig. 1. DEA channels corresponding to the observed fragment ions, along with their threshold energies, are summarized in Table I. The threshold energies are derived from the thermodynamic dissociation energies and electron affinities of the relevant species as follows: the thermodynamic heat of formation is 2.58 eV[76] for O and 1.48 eV[77] for O_3 (supplementary material, Section S2). The electron affinities of O, O_2, and O_3 are 1.46,[78] 0.44,[79] and 2.1 eV,[80] respectively.

First resonance

The momentum image of O_2^- recorded at an incoming electron energy of 1.6 eV, shown in Fig. 2(a), exhibits a central low-KE distribution. From this image, the KE distribution for the O_2^- channel is determined to be in the range 0–0.15 eV, which corresponds to the KER of 0–0.45 eV (supplementary material, Section S3). The thermodynamic threshold for O_2^- formation, with the neutral O fragment in the $^3P_2$ state, is 0.66 eV as given in Table I, indicating that the energy partitioned into the internal excitation of the O_2^- fragment is in the range 0.94–0.49 eV. We attribute the internal excitation to vibrational excitation of the O_2^- ion with very

TABLE I. DEA fragmentation channels and their thermodynamic thresholds.

S.No.	Fragmentation channel	Thermodynamic threshold (eV)
1	$O_3 + e^- \rightarrow O^- \left(^2P\right) + O_2\left(X^3\Sigma_g^-\right)$	−0.36
2	$O_3 + e^- \rightarrow O^- \left(^2P\right) + O_2\left(a^1\Delta_g\right)$	0.62
3	$O_3 + e^- \rightarrow O^- \left(^2P\right) + O_2\left(b^1\Sigma_g^+\right)$	1.27
4	$O_3 + e^- \rightarrow O^- \left(^2P\right) + O_2\left(c^1\Sigma_u^-\right)$	3.74
5	$O_3 + e^- \rightarrow O^- \left(^2P\right) + O_2\left(A'^3\Delta_u\right)$	3.94
6	$O_3 + e^- \rightarrow O^- \left(^2P\right) + O_2\left(A^3\Sigma_u^+\right)$	4.03
7	$O_3 + e^- \rightarrow O^- \left(^2P\right) + O_2\left(B^3\Sigma_u^-\right)$	5.81
8	$O_3 + e^- \rightarrow O_2^- \left(X^2\Pi_g\right) + O\left(^3P\right)$	0.66
9	$O_3 + e^- \rightarrow O_2^- \left(X^2\Pi_g\right) + O\left(^1D\right)$	2.63
10	$O_3 + e^- \rightarrow O_2^- \left(X^2\Pi_g\right) + O\left(^1S\right)$	4.85
11	$O_3 + e^- \rightarrow O^- \left(^2P\right) + O\left(^3P\right) + O\left(^3P\right)$	4.76

12 October 2026 11:14:18

Published under an exclusive license by AIP Publishing

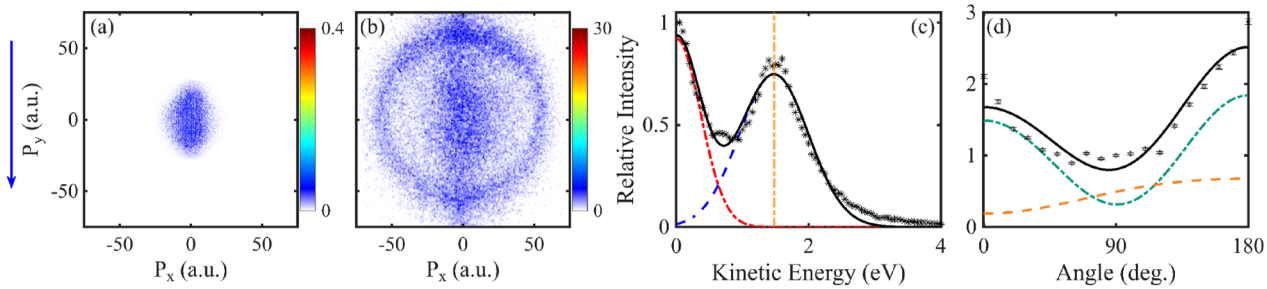


FIG. 2. Momentum image of (a) O_2^- at 1.6 eV and (b) O^- at 1.8 eV, with the blue arrow indicating the direction of the electron beam. (c) Corresponding KE distribution of O^- with the fit using Gaussian functions. The vertical line marking the peak position of the Gaussian at 1.45 eV. (d) Angular distribution for the O^- ions for the KE window of 1.1–1.8 eV. The angular distribution data, normalized at 90° with respect to the electron beam, are fitted (black solid line) with contributions from B_2 (green dashed–dotted line) and A_1 (orange dashed line) states.

little rotational excitation. We conclude this based on the following discussion. This is because O_3^- is known to exhibit three well-characterized low-lying electronic excited states of $^2B_2$, $^2A_2$, and $^2A_1$ symmetries[54,81] as outlined in Table II. Hiller *et al.* have experimentally determined the energies of the optically allowed $^2A_2$ and $^2A_1$ states through photodissociation of O_3^- ions, locating them at −0.053 and 0.557 eV relative to the ground state O_3 (X^1A_1), respectively.[54] Peterson *et al.* calculated the energy of the $^2B_2$ state to be −0.803 eV.[81] Each of these three excited states can be accessed at an incident electron energy of ~ 1.6 eV, depending on the strength of the Franck–Condon overlap. All these states are characterized by the occupancy of two electrons in the b_1 orbital. This b_1 orbital is a π- type orbital, which is antibonding along the O – O bonds but bonding along the terminal O atoms. This implies that these anionic states most likely lead to two-body fragmentation via a symmetric dissociation mechanism, in which the central oxygen atom dissociates to form neutral O, while the terminal oxygens approach each other to form a vibrationally excited O_2^-. This process is facilitated by the combination of symmetric stretch and bending vibration modes of the anionic parent, similar to that observed in DEA to OClO[17] and SO_2[18]. Therefore, symmetric dissociation of O_3^- produces vibrationally excited yet kinetically thermal fragments, consistent with our observed mechanism, as noted by Allan *et al.*[51] and Walker *et al.*[24] However, it should be noted that O_2^- can sustain a maximum vibrational energy of 0.44 eV before reaching its autodetachment threshold. Consequently, a significant fraction of the O_2^- anions are expected to undergo autodetachment, rendering them undetectable in our measurements. This autodetachment limit cannot be probed because the spectrometer's energy resolution is limited at low energies, compounded by the intrinsic spread in the incident electron energy distribution. Allan *et al.* have reported the presence of these auto-detaching vibrationally excited O_2^- at this energy, corroborating the instability of these states through the measured KE of the auto-detaching electrons.[52] Based on the observed KER for this channel, the dissociation threshold of 0.66 eV, and the 0.44 eV autodetachment limit, we conclude that the observed KE distribution of O_2^- ions results from attachment of electrons with energies <1.6 eV. The upper limit of the observed KE corresponds to DEA of electrons with energies between 1.1 and 1.55 eV. The corresponding internal excitation of the O_2^- fragment is from $v = 0$ to 3, respectively. The zero-KE ions would arise from the DEA from electrons with energies between 0.66 and 1.1 eV, again with the ion fragment excitation in the range $v = 0$ to 3, respectively. This is consistent with the finite energy width of our electron beam, which is 0.5 eV FWHM, and the DEA cross section peak around 1.1 – 1.2 eV for the O_2^- channel.[45,51,53] The observed KE distribution that peaks at zero

TABLE II. NIRS of O_3^- obtained by different theoretical calculations, experimental observations, and their positions with respect to the neutral and anion ground states. The experimental observation by Arnold *et al.* for (X^2B_1) has been taken as the reference for the corresponding value calculation of the energy position with respect to O_3 (X^1A_1) or with respect to O_3^- (X^2B_1) when only one of the values is available.

Symmetry	Energy with respect to O_3 (X^1A_1) (eV)	Energy with respect to O_3^- (X^2B_1) (eV)
X^2B_1	−2.103[a]	0
$^2B_2$	−0.803	1.3[b]
$^2A_2$	−0.053	2.05[c]
$^2A_1$	0.557	2.66[c]
$^2A_1$	0.177, 0.277	2.28[d], 2.38[e]
$^2B_2$	0.157, 0.147	2.26[d], 2.25[e]
$^2A_2$	0.747, 0.763	2.85[d], 2.87[e]
$^2A_1$	1.03[f]	3.133
$^2B_2$	1.18[f]	3.283
$^2A_2$	2.08[f]	4.183
$^2A_1$	4.2[g], 4.83[f]	6.303, 6.933
$^2B_2$	6.6[g]	8.703
$^2B_1$	7.30[f]	9.403
$^2A_1$	7.60[h]	9.703
$^2B_2$	8.57[f]	10.673

[a] Arnold *et al.*[80]
[b] Peterson *et al.*[81]
[c] Hiller *et al.*[54]
[d] Koch *et al.*[83]
[e] Rangwala *et al.*[53]
[f] Nestmann *et al.*[55]
[g] Allan *et al.*[51]
[h] Curik *et al.*[68]

12 October 2026 11:14:18

Published under an exclusive license by AIP Publishing

eV is partly due to the convolution of the absolute cross section curve for this channel and the electron energy profile of the gun with the mean at 1.6 eV, and partly due to bias of the parallel slice imaging toward the low-energy, particularly toward thermal energy fragments.[82] This is entirely possible in our case, as the electron beam with a 1.6 eV central energy has a 0.5 eV FWHM energy distribution. This is consistent with the high-resolution DEA measurements of this ion.[44,51,52]

Figure 2(b) shows the momentum image of O^- obtained at an incident electron energy of 1.8 eV. A similar, but more diffuse, low-energy distribution to that of O_2^- along with an additional outer ring is visible in this image. However, the size of the O^- inner low-energy distribution does not increase proportionally with the incident electron energy, indicating a relatively smaller increase in KE, as described in the supplementary material, Section S4. The thermodynamic threshold for O^- formation from neutral O_3 $(X^3\Sigma_g^-)$ is −0.36 eV (Table I). Therefore, for an incident electron energy of 1.8 eV, the total excess energy available in the system is ~2.16 eV. The normalized KE distribution of O^- ions is calculated from the momentum image in Fig. 2(b) and presented in Fig. 2(c). The contribution from ions corresponding to the inner low-KE region is represented by the red dotted–dashed curve, which peaks near zero KE with a HWHM of ~0.45 eV. Since the incoming electron energy is below the three-body fragmentation threshold of 4.76 eV (Table I), the KER of the inner distribution, obeying momentum conservation of the two-body dissociation, is estimated to be ~0.68 eV (at HWHM). This leaves roughly 1.48 eV available for the internal excitation of O_2 fragments, which is sufficient to promote O_2 to $a^1\Delta_g$ state or $b^1\Sigma_g^+$ state (for KER < 0.53 eV, i.e., KE < 0.35 eV), as indicated by the threshold energy in Table I. Alternatively, the well depth of 5.12 eV[84] for O_2 in its $X^3\Sigma_g^-$ state can accommodate 1.54 eV within its vibrational degrees of freedom, while the molecule remains in the electronic ground state. The latter is the most likely scenario upon symmetric dissociation via bending-mode excitation, similar to the O_2^- channel, in which the middle O atom dissociates as O^-. The vibrational excitation in this case is primarily governed by the degree of bending-mode excitation relative to the symmetric stretch mode. Therefore, a significant portion of the available energy is dissipated into the vibrational degrees of freedom of O_2, resulting in fragments with comparatively low KE. Moreover, depending upon competition between symmetric stretch and bending modes of vibrations, additional excess energy in the symmetric dissociation dynamics will result in further enhancement in vibrational excitation of O_2, as the corresponding KER will not show an equivalent increment. For higher incident electron energies, if the dissipation in the symmetric stretch mode is less than that of the bending modes, O^- arising from the central atom of the parent anion will acquire a relatively lower increment in the KER of this channel and a higher vibrational excitation of the O_2 moiety. This is consistent with our earlier observation where the size of the inner distribution in the O^- momentum image does not show the expected proportional increment with the electron energy. These observations indicate that both O_2^- and low-energy O^- ions originate from the same NIRS through a symmetric dissociation mechanism.

The presence of an additional outer ring in the momentum image at 1.8 eV, as shown in Fig. 2(b), indicates the possible presence of an additional dissociation pathway. A comprehensive kinematic analysis of momentum images in this energy range is crucial to investigate the additional dissociation pathway. The KE of the outer ring peaks near 1.45 eV, presented as a blue dashed curve in Fig. 2(c), corresponding to a KER peaking around 2.17 eV in the two-body fragmentation channel. This nearly equals the available excess energy (~2.16 eV), suggesting minimal energy transfer to the internal modes of the O_2 fragment. This indicates that this dissociation is rapid and proceeds via the asymmetric dissociation pathway, akin to the O^- channel observed in DEA to both OClO[17] and SO_2[18].

Since almost all of the excess energy is taken up by the translational degrees of the fragments, O_2 does not undergo significant rotation before dissociation, validating the use of the axial recoil approximation. Therefore, the angular distribution of O^- may directly reveal the electron capture probability of O_3 with respect to the incoming electron beam direction, and we can determine the symmetry of the NIRS of O_3^- contributing to the $O^- + O_2$ $\left(X^3\Sigma_g^-\right)$ channel. Using the formalism developed by O'Malley and Taylor[85] for diatomic molecules, later extended by Azria *et al.*[86] for polyatomic species, we can determine the symmetry of the NIRS state, as described in our earlier studies.[17,18] The angular distribution of the fragment ions is expressed as

$$I(\theta)\ \alpha\ \frac{1}{2\pi}\int_0^{2\pi}\left|\sum_{ml\varepsilon}^{\infty} i^l\ \exp\ (i\delta_l)\ a_{lm}^{\epsilon}\ \chi_{lm}^{\epsilon^*}(\theta,\varphi)\right|^2 d\varphi,$$

where $\chi_{lm}^{\epsilon^*}(\theta,\ \varphi)$ is the basis function for the irreducible representation of the molecular point symmetry group, a_{lm}^{ϵ} denotes its amplitude, and δ_l is the associated phase. The angles (θ,φ) define the orientation of the dissociating bond with respect to the incident electron beam. These functions are expressed in the molecular (dissociation) frame and, through appropriate transformations from the laboratory to the molecular frame, they can be represented as linear combinations of spherical harmonics. For the cases where a single NIRS cannot adequately reproduce the measured angular distribution, contributions from multiple NIRSs are included and combined incoherently. The form of the angular distribution function used for fitting is given by

$$I(\theta) = \sum_i a_i I_i(\theta),$$

where $I_i(\theta)$ corresponds to the angular distribution function for a given NIRS and a_i corresponds to its weight factor. The choice of NIRSs and the terms included in the fits are based on physical considerations and analysis described in Section S5 of the supplementary material.

The outer ring in Fig. 2(b) exhibits a clear forward–backward asymmetry, with higher intensity in the backward direction and approximately half that intensity perpendicular to the electron beam. This asymmetry is clearly reflected in the corresponding angular distribution shown in Fig. 2(d). Since the O_3 molecule lacks inversion symmetry about the dissociation axis, coherent contributions of even and odd partial waves may manifest in the observed asymmetry in the angular distribution. O_3, belonging to the C_{2v} symmetry group, has a neutral ground state of X^1A_1 with an equilibrium bond angle of 116.8. Rangwala *et al.* proposed that the $^2A_2$ and $^2B_2$ states may govern DEA to O_3 at approximately 1.4 eV, consistent

12 October 2026 11:14:18

Published under an exclusive license by AIP Publishing

with electron-capture selection rules.[53] In contrast, *R*-matrix calculations by Nestmann *et al.* suggested that the broad $^2A_2$ Feshbach resonance, being two orders of magnitude wider than the $^2A_1$ and $^2B_2$ resonances, mainly accounts for the 1.3 eV peak.[55] Therefore, in principle, a linear combination of spherical harmonics corresponding to transitions from X^1A_1 to the $^2A_1$, $^2B_2$, and $^2A_2$ states of O_3^- can be used for fitting the angular distribution. However, the characteristic intensity of the $^2A_2$ transition is dominant perpendicular to the electron beam. Since the experimentally observed angular distribution in Fig. 2(d) clearly shows intensity predominantly along the beam direction, with a preference for backward scattering, the fitting was performed using a linear combination of only $^2A_1$ and $^2B_2$ states. The partial wave fit results indicate the contribution from the $^2B_2$ state is about twice as strong as that from the $^2A_1$ state. The extensive partial wave analysis, as discussed in the supplementary material, Section S5, shows that although the angular distribution gets a majority contribution from the $^2B_2$ states, it alone cannot provide a complete picture, even if higher partial waves are included. Based on these observations, we propose that the NIRS undergoes a rapid asymmetric dissociation mechanism that leads to the formation of the O^- outer ring with negligible internal excitation of the O_2 fragment.

DEA from the second resonance

The momentum image of O^- recorded at an incident energy of 3.4 eV exhibits a single, well-defined ring structure as shown in Fig. 3(a), indicating that a single dissociation pathway dominates in this energy range. The total excess energy, assuming the lowest threshold dissociation channel, at this electron energy is ~3.76 eV. The corresponding KE distribution, shown in Fig. 3(b), peaks around 1.8 eV. The non-zero intensities near 0 eV (red dashed–dotted curve) are attributed to the early onset of the ~6.5 eV resonance of O_2^- arising from the O_2 impurity in the effusive beam. Therefore, the estimated KER for this two-body channel obeying momentum conservation is ~2.7 eV, indicating ~1.06 eV energy dissipation into ro-vibrational excitation of the molecular fragment of O_2 in its electronic ground state ($X^3\Sigma_g^-$). The relatively large KER suggests an active asymmetric dissociation mechanism. Asymmetric dissociation reflects dominant excitation of the asymmetric stretch mode, leading to rapid bond cleavage and imparting an impulsive torque to the O_2 fragment. This may result in pronounced rotational excitation, with most of the excess energy converted into translational KE. The extent of O_2 rotation depends on the instantaneous bond angle during dissociation, the O^- momentum, and the fragment's mass ratio. Under the simple impulse approximation, we assume that the bond length of the diatomic fragment remains unchanged during the instantaneous dissociation of the other bond (see the supplementary material, Section S6). Assuming dissociation occurs near the equilibrium geometry, the rotational energy of the molecular fragment is estimated to be $\frac{1}{4.7}$ of the excess energy. Hence, the excess energy of ~3.76 eV in the O_3^- system would result in rotational excitation of ~0.80 eV, leaving ~0.26 eV for the vibrational excitation. Therefore, a total of ~1.06 eV of energy is dissipated in ro-vibrational excitation of the molecular fragment of O_2 in $X^3\Sigma_g^-$ states undergoing an asymmetric dissociation mechanism. Notably, in this case, although the molecular fragment is ro-vibrationally excited, the vibrational excitation would be only up to $v = 3$. On the other hand, the rotational excitation would be the result of the impulse imparted during dissociation. This would make the axial-recoil approximation still valid for the angular distribution. At 3.4 eV electron energy, the second channel of O^- can also be accessed, where the O_2 molecular fragment is electronically excited to the $a^1\Delta_g$ state. In this channel, with a thermodynamic threshold of 0.62 eV, the excess energy in the system would be 2.78 eV, which matches very well with the observed KER. In this case, the axial recoil

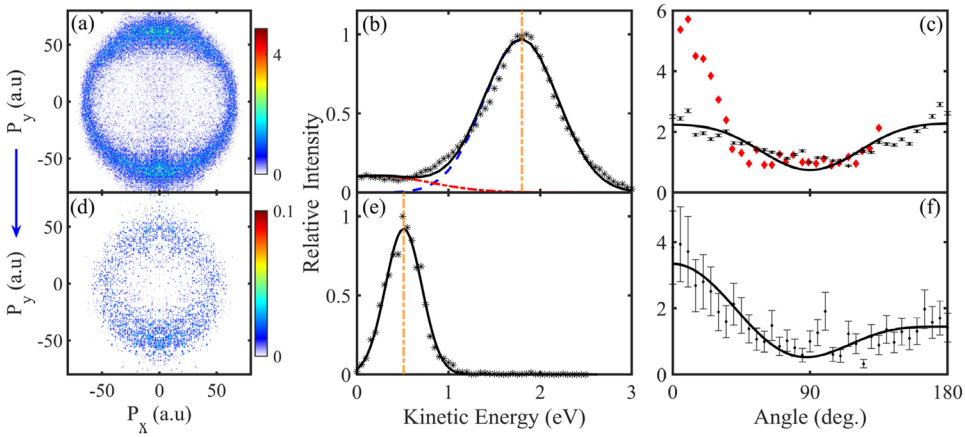


FIG. 3. (a) Momentum image of O^- at 3.4 eV electron energy and (b) corresponding KE distribution of O^- with a fit using a Gaussian function. The vertical line marks the peak position of the Gaussian at 1.8 eV. (c) Angular distribution of the ions in the KE range 1.65–2.05 eV. In addition, the angular distribution fit (black solid line) considers the B_2 state as the NIRS, along with the angular distribution data reported by Allan *et al.* (red diamond).[51] (d) Momentum image of O_2^- at 3.1 eV electron energy. (e) Corresponding KE distribution with the fit using a Gaussian function. The vertical line marks the peak position of the Gaussian at 0.51 eV. (f) Angular distribution of the ions in the KE range 0.3–0.7 eV. In addition, the angular distribution fit (black solid line) considers the B_2 state as the NIRS. The electron beam direction for the momentum images is from top to bottom. The 180°–360° hemisphere of the momentum images is generated by mirror reflection of the measured 0°–180° hemisphere for presentation.

12 October 2026 11:14:18

Published under an exclusive license by AIP Publishing

approximation would be valid, and we can obtain the symmetry of the NIRS participating in this process.

The single distinct ring-like feature observed in the momentum image of the O^- channel at 3.4 eV, shown in Fig. 3(a), exhibits maximum intensity along the electron-beam direction with no forward–backward asymmetry. The corresponding angular distribution is obtained from Fig. 3(a) and presented in Fig. 3(c). We tried fitting the angular distribution using single NIRS of various symmetries and found that the NIRS with B_2 symmetry, including the p and d partial waves (the lowest allowed partial waves), gave the best possible fit, as shown in Fig. 3(c). Allan *et al.* reported more pronounced intensities at the forward direction, which led them to attribute this feature to the involvement of A_1 symmetry in this energy range.[51] They argued that the observed angular distribution could arise from maximum overlap between the plane wave of the incident electron and the A_1 orbital. At the same time, they also suggested that the possible vibronic coupling of this resonance with the B_2 NIRS could make the dissociation efficient. Further support for the involvement of a B_2 NIRS comes from Allan *et al.*'s observation of substantial excitation of the asymmetric vibrational mode in the electron energy-loss spectrum around 3.9 eV. By symmetry arguments, the asymmetric vibrational mode, which has B_2 symmetry, will be excited by the resonance of the same symmetry, i.e., B_2 symmetry, if the partial waves other than the s-wave are scattered. Notably, the asymmetric vibrational mode is likely to play a crucial role in the asymmetric dissociation mechanism proposed here. Taken together, these observations and our findings, we conclude that the $^2B_2$ NIRS of O_3^- contributes to the DEA signal at this energy as against the previously inferred $^2A_1$ state, leading to the formation of O^- with electronically excited $O_2\left(a^1\Delta_g\right)$ or $O_2\left(X^3\Sigma_g^-\right)$ fragments with 1.06 eV in ro-vibrational excitation.

The momentum image of O_2^- recorded at 3.1 eV is presented in Fig. 3(d). Similar to the previously discussed O^- momentum image, Fig. 3(d) reveals a single ring-like distribution, suggesting only one dissociation pathway is active in this energy range. For the incident electron energy of 3.1 eV, the excess energy in the system for this channel would be ~ 2.44 eV for channel 8 and 0.47 eV for channel 9 in Table I. This limits channel 9's contribution to the KE value of 0.16 eV. The KE distribution obtained from the momentum image is shown in Fig. 3(e), which peaks around 0.51 eV, indicating an estimated KER for this channel of ~1.53 eV. Hence, we conclude that this DEA signal is from channel 8, where the O atom is in its ground state. Consequently, the remaining ~0.91 eV is partitioned into the ro-vibrational modes of O_2^- $(X^2\Pi_g)$. A similar analysis under the simple impulse approximation estimates that the excess energy of ~2.44 eV in the O_3^- system would result in rotational excitation of ~0.52 eV, undergoing a similar asymmetric dissociation mechanism active for the O^- channel in this energy range. Therefore, vibrational excitation in O_2^- is expected to be ~0.39 eV. Considering the autodetachment threshold of 0.44 eV of O_2^-, any higher vibrational excitation would lead to electron ejection, rendering them undetectable, which is consistent with previous observations.[52]

In addition, as seen in Fig. 3(d), the O_2^- momentum image exhibits a more pronounced forward intensity, with nearly isotropic intensity in other angles. The corresponding angular distribution presented in Fig. 3(f) is fitted solely by the $^2B_2$ NIRS within the C_{2v} point group symmetry of O_3^-. Here, the forward angle preference over all other angles is explained by contributions from p and d partial waves of the B_2 symmetry. A detailed comparison of the quantitative contributions of each partial wave for different states is presented in the supplementary material, Section S5. Walker *et al.* have proposed that both the O^- + O_2 and O_2^- + O channels arise from the same NIRS of O_3^- through asymmetric dissociation, supporting a unified dissociation pathway.[24] We, therefore, conclude that the same $^2B_2$ NIRS of O_3^- contributes to the DEA signal in the 3.1 – 3.4 eV region via rapid asymmetric dissociation, leading to the formation of O^- with O_2 with either ro-vibrational or electronic excitation or O_2^- with vibrational excitation up to $v = 3$ and the remaining energy in its rotational excitation with the O atom in its ground state.

Figures 4(a) and 4(d) show momentum images of the O^- and O_2^- channels obtained at 4.4 and 4.1 eV, respectively. Both momentum images primarily feature a single distinct ring, indicating a single dissociation mechanism. The O^- ion KE distribution peaks at ~2 eV, indicating a KER of ~3 eV for this channel, while O_2^- ion KE peaks at ~ 0.8 eV, indicating a ~2.4 eV KER for this channel, owing to momentum conservation in two-body dissociation. Based on the threshold energies shown in Table I, the available excess energies in the O^- production are estimated to be 4.76, 3.78, 3.13, 0.66, 0.46, and 0.37 eV for channels 1–6, respectively. Similarly, the available excess energies in the O_2^- production would be 3.44 and 1.47 eV for channels 8 and 9 from Table I, respectively. Based on the observed KER, we eliminate the last three channels for the O^- production and channel 9 for the O_2^- production at these energies. The simple impulse approximation, considering the asymmetric dissociation, estimates a rotational excitation of ~1.01 and ~0.73 eV of the molecular fragment in O^- formation from the 1st channel and O_2^- from the 8th channel from Table I, respectively. Therefore, the vibrational excitation of O_2 in $O^- + O_2\left(X^3\Sigma_g^-\right)$ and O_2^- in $O\left(^3P\right) + O_2^-$ channels would be ~0.75 and ~0.31 eV, respectively. For the O^- ions, the channels 2 $(O^- + O_2\ \left(a^1\Delta_g\right))$ and 3 $(O^- + O_2\ \left(b^1\Sigma_g^+\right))$ may also contribute with lower internal excitation (0.78 and 0.13 eV, respectively) of the O_2 fragment. As argued earlier, in all these cases the axial-recoil approximation would be applicable to various degrees. In addition, the O^- momentum image in Fig. 4(a) appears to have a faint thermal structure in the center. This thermal structure in the center manifests as a peak around 0 eV, represented by the red dotted–dashed curve in Fig. 4(b). We attribute this feature to the well-known early onset of O^- from the O_2 impurity, peaking around 6.5 eV electron energy since the thermodynamic threshold for these channels is 3.7 eV. Therefore, a similar thermal peak is not observed in the corresponding O_2^- channel from DEA to O_3.

A pronounced forward–backward asymmetry re-emerges in the O^- channel, with enhanced intensity in the backward direction, as shown in Fig. 4(a). In contrast, the momentum image of O_2^- exhibits a stronger forward–backward asymmetry, with greater intensity in the forward direction, as shown in Fig. 4(d). The angular distributions of the O^- and O_2^- channels extracted from these momentum images are shown in Figs. 4(c) and 4(f), respectively. Both of these angular distributions are fitted with a linear combination of $^2A_1$ and $^2B_2$ NIRSs, indicating that, for O^- formation, both symmetries contribute nearly equally, whereas in the O_2^- channel, the B_2 state contributes approximately twice as much as the A_1 state.

12 October 2026 11:14:18

Published under an exclusive license by AIP Publishing

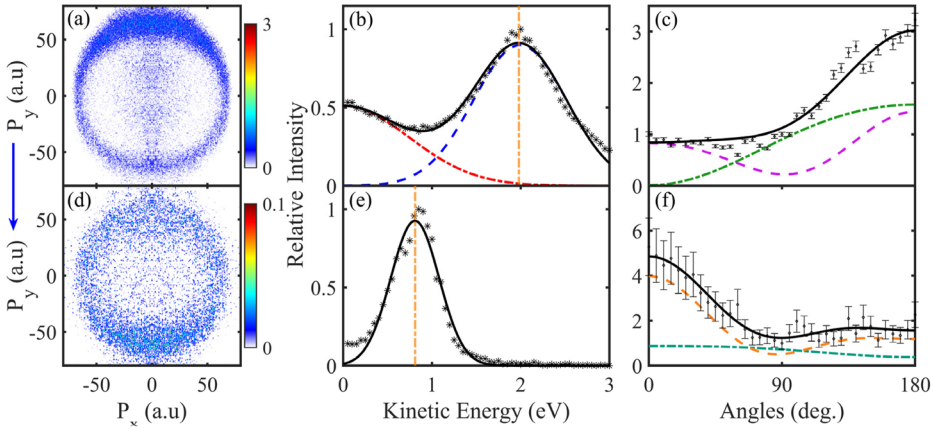


FIG. 4. (a) Momentum image of O^- at 4.4 eV. (b) Corresponding KE distribution with the fit using Gaussian functions. The vertical line marks the peak position of the Gaussian at 2 eV. (c) Angular distribution of the O^- ions in the KE range 1.8–2.20 eV. In addition, the fits to the data (black solid line) using NIRSs of B_2 (magenta dashed line) and A_1 (burgundy dashed–dotted line) symmetries. (d) Momentum image of O_2^- at 4.1 eV. (e) Corresponding KE distribution with the fit using Gaussian functions. The vertical line marks the peak position of the Gaussian at 0.8 eV. (f) Angular distribution of the O_2^- ions in the energy range 0.7–1.1 eV. In addition, the fits to the data (black solid line) using NIRSs of B_2 (orange dashed line) and A_1 (green dashed–dotted line) symmetries. The electron beam direction in the momentum images is from top to bottom. The 180°–360° hemisphere of the momentum images is generated by mirror reflection of the measured 0°–180° hemisphere for presentation.

It is worth noting that the angular distribution of the O_2^- ions can be reasonably reproduced by considering the B_2 contribution alone. However, for the O^- channel, the measured angular distribution cannot be adequately reproduced by the B_2 contribution alone and requires a significant contribution from A_1 state. Interestingly, the momentum images of the O^- and O_2^- channels at this energy exhibit complementary angular distributions, indicating that the same NIRS states may be undergoing similar dissociation mechanism with electron charge localization in the two different moieties. A qualitative energy analysis of this dissociation dynamics is discussed in Section S7 of the supplementary material. The details of these fits are given in the supplementary material, Section S5. These results indicate that the $^2B_2$ state, which was present in the previous resonance, continues to have a considerable contribution in both channels, along with the appearance of a new anionic state of $^2A_1$ symmetry in this energy range. Using Koopmans' theorem, Allan *et al.* proposed the existence of a $^2A_1$ symmetry resonance at ~4.2 eV (see Table II), arising from the temporary capture of the incident electron into σ^* orbitals that are strongly antibonding along the O – O bond.[5,51] This is experimentally verified by our measured angular distributions. Therefore, we conclude that the $O^- + O_2$ and $O + O_2^-$ channels originate from common O_3^- resonance states of $^2B_2$ and $^2A_1$ symmetry, undergoing an asymmetric dissociation leading to the formation of O_2 and O_2^- with ro-vibrational excitation.

Analysis of DEA from the third peak

Contaminations from residual O_2 have posed challenges in obtaining reliable momentum images for the O^- channel in the third resonance region near 7.5 eV. Nevertheless, the momentum image of O_2^- recorded at 6.9 eV presented in Fig. 5(a), remains unaffected by this impurity. If O_2^- is produced with O (^3P), an excess ~6.24 eV energy is available. The corresponding KE distribution peaks

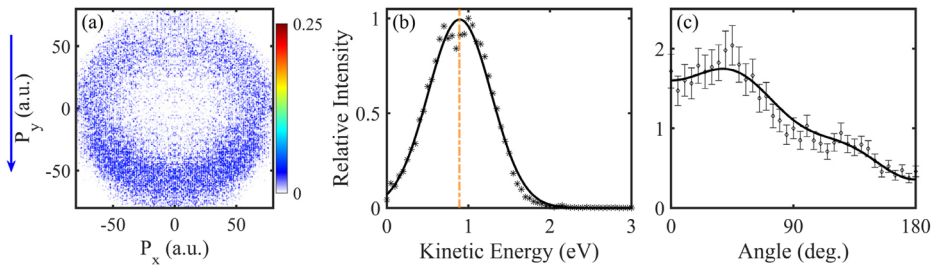


FIG. 5. (a) Momentum image of (a) O_2^- at 6.9 eV, with the blue arrow indicating the direction of the electron beam. (b) Corresponding KE distribution of O_2^- with a fit using a Gaussian function. The vertical line marks the peak of the Gaussian at 0.9 eV. (c) Angular distribution for the O^- ions for the KE window of 0.6–1.2 eV. The angular distribution data, normalized at 90° with respect to the electron beam, are fitted (black solid line) with NIRS of A_1 symmetry. The 180°–360° hemisphere of the momentum images is generated by mirror reflection of the measured 0°–180° hemisphere for presentation.

12 October 2026 11:14:18

Published under an exclusive license by AIP Publishing

around 0.9 eV as shown in Fig. 5(b), indicating the expected KER to be ~2.7 eV, and remaining ~3.54 eV for internal excitation of O_2^-. This energy is adequate to populate the low-lying O (^1D) state but insufficient to access the O (^1S) state. Based on the energetics from Table I, the O_2^- ($X^2\Pi_g$) + O (^1D) channel is estimated to have an excess energy of ~4.27 eV. Here, the internal excitation of O_2^- would be ~1.57 eV. Using the simple impulse model, the vibrational excitation of O_2^- will be 0.66 eV, and the rotational excitation will be 0.91 eV. Since O_2^- can accommodate only up to 0.44 eV in its vibrational degrees of freedom, at least 1.13 eV of the internal energy must be partitioned into rotational excitation. This substantially exceeds the rotational energy predicted by the simple impulse model, indicating the presence of dissociation dynamics beyond the scope of the model. In addition, the angular distribution of O_2^- ions presented in Fig. 5(c) exhibits a pronounced forward–backward asymmetry favoring the forward direction of the electron beam.

Partial-wave analysis reveals that the observed angular distribution can be fully described by including only the *s*-, *p*-, and *d*-wave contributions of NIRS with $^2A_1$ symmetry. The details of the angular distribution fits are discussed in Section S5 of the supplementary material. A similar two-peaked angular distribution was observed in the DEA of H^- ions from H_2O at 8.5 eV,[87] which is known to be a two-particle-one-hole type Feshbach resonance of $^2A_1$ symmetry. The assignment of this $^2A_1$ resonance at 6.9 eV in O_3^- is interesting, as theoretical studies predict a $^2B_2$ shape resonance at 6.6 eV[51] and a $^2B_1$ Feshbach resonance near 7.3 eV.[55] The absence of the $^2B_1$ resonance in the present measurements may be attributed to its theoretically predicted ultrashort lifetime (~11 fs), which is likely insufficient for the resonance to survive autodetachment and undergo dissociation.[55] The *ab initio* calculations by Curik *et al.* predicts an A_1 broad shape resonance at 7.6 eV with a large width of 2.5 eV. This translates to a lifetime of ~0.3 fs, which is too short to effectively compete against autodetachment.[68] Therefore, to sustain DEA in this high-energy region, the NIRS is expected to be either a Feshbach resonance or a two-particle-one-hole shape resonance. We propose that this resonance near 6.9 eV is a Feshbach resonance, as predicted by Allan *et al.*,[51] while the measured angular distribution indicates that this Feshbach resonance is of A_1 symmetry.

CONCLUSION

We have investigated symmetry-driven dynamics in DEA to O_3 by measuring the kinetic-energy and angular distributions of $O^- + O_2$ and $O_2^- + O$ channels over a broad incident electron-energy range of 0 – 10 eV using the VSI methodology. The O_2^- yield exhibits resonances at 1.2, 3.0, and 7.3 eV, whereas the dominant O^- channel peaks at 1.4 and 3.0 eV. These results reveal that DEA to O_3 proceeds through a competition between symmetric dissociation and asymmetric dissociation. The symmetry of the NIRSs governing the asymmetric dissociation pathways are identified by partial wave analysis of the measured angular distribution. Near the lowest peak at 1.2 eV, symmetric dissociation is identified in both O^- and O_2^- channels, where the excitation of symmetric stretch and bending modes leads to cleavage of the central oxygen atom, producing vibrationally excited O_2 and O_2^- molecular moieties with thermal KE. Due to the autodetachment threshold, O_2^- can be produced with a maximum of 0.44 eV in its vibrational degrees of freedom, whereas the O_2 moiety is observed with ~1.54 eV vibrational excitation. In addition, an asymmetric dissociation has been identified in the O^- channel, where overlapping $^2A_1$ and $^2B_2$ NIRSs result in enhanced translational energy and negligible internal excitation of the O_2 moiety. The contributions from the $^2A_1$ and $^2B_2$ NIRSs are found to be in the ratio of 1 : 2.

In the second resonance region (3.1 – 3.4 eV), both the O^- and O_2^- ions originate from a common O_3^- resonance via the asymmetric dissociation mechanism, demonstrating a single NIRS with $^2B_2$ symmetry. In this regime, O_2 is formed in the electronically excited state $\left(a^1\Delta_g\right)$ or with ~ 1.06 eV in ro-vibrationally excited $O_2\left(X^3\Sigma_g^-\right)$, whereas O_2^- is formed with 0.91 eV in ro-vibrational excitations. In the intermediate region (4.1 – 4.4 eV), both $^2A_1$ and $^2B_2$ resonances contribute with ~1 : 1 and ~1 : 2 ratios, again driving asymmetric dissociation into $O^- + O_2$ and $O_2^- + O$, respectively. The molecular moieties are observed to have significantly enhanced ro-vibrational excitation of ~1.76 eV for O_2 and ~1.04 eV for O_2^-. This provides experimental evidence of the earlier proposed $^2A_1$ shape resonance at 4.2 eV.[51]

In the third resonance region (6.6 – 7.5 eV), the angular distributions of O_2^- exhibit a strong forward–backward asymmetry. Despite the theoretical predictions of a nearby $^2B_2$ shape resonance at ~6.6 eV, a partial-wave analysis shows that the $^2A_1$ anionic state overwhelmingly dominates at 6.9 eV. We propose this resonance to be a Feshbach resonance, as predicted by Allan *et al.*[51] These results establish a comprehensive understanding of DEA dynamics, involving competing symmetric dissociation and asymmetric dissociation mechanisms leading to the formation of highly internally excited species, which are highly reactive and may be important in the reaction chemistry of the cold interstellar medium. These findings highlight the need for advanced *ab initio* calculations along with time-resolved studies to probe these coupled electronic–nuclear dynamics.

SUPPLEMENTARY MATERIAL

See the supplementary material for detailed information on the preparation of ozone, the partial-wave equations used to fit the angular distributions, and the corresponding fit results. The material also includes a derivation of the rotational energy transferred to the diatomic fragment during dissociation, along with other supplementary material.

ACKNOWLEDGMENTS

K.G. acknowledges support for an extended visit to the Molecular Physics Laboratory at the Open University and a SEED grant from IISER Thiruvananthapuram. VSP acknowledges the financial support from the Department of Atomic Energy, India, under Project Identification No. RTI4012. N.J.M. acknowledges support from the FP7 European project ITN Lassie Grant Agreement No. 238258 during the development of this study and the H2020 Twinning project "Achievement of Excellence in Electron Processes for Future Technologies" (ELEvaTE) Grant Agreement No. 692335 for collaborative discussions.

12 October 2026 11:14:18

Published under an exclusive license by AIP Publishing

AUTHOR DECLARATIONS

Conflict of Interest

The authors have no conflicts to disclose.

Author Contributions

Melvin Varghese and Dharun J. contributed equally to this paper.

Melvin Varghese: Conceptualization (equal); Formal analysis (equal); Investigation (equal); Validation (equal); Visualization (equal); Writing – original draft (equal); Writing – original draft (equal). **Dharun J**: Conceptualization (equal); Formal analysis (equal); Investigation (equal); Validation (equal); Visualization (equal); Writing – original draft (equal); Writing – original draft (equal). **Nigel J. Mason**: Conceptualization (equal); Funding acquisition (equal); Resources (equal); Validation (equal); Writing – original draft (equal). **E. Krishnakumar**: Conceptualization (equal); Investigation (equal); Methodology (equal); Validation (equal); Visualization (equal); Writing – original draft (equal). **Vaibhav S. Prabhudesai**: Conceptualization (equal); Formal analysis (equal); Project administration (equal); Supervision (equal); Validation (equal); Visualization (equal); Writing – original draft (equal); Writing – original draft (equal). **Krishnendu Gope**: Conceptualization (equal); Data curation (equal); Formal analysis (equal); Investigation (equal); Methodology (equal); Project administration (equal); Supervision (equal); Validation (equal); Visualization (equal); Writing – original draft (equal); Writing – original draft (equal).

DATA AVAILABILITY

The data that support the findings of this study are available from the corresponding authors upon reasonable request.

REFERENCES

[1] M. N. R. Ashfold *et al.*, "Exploring nuclear motion through conical intersections in the UV photodissociation of phenols and thiophenol," Proc. Natl. Acad. Sci. U.S.A. **105**, 12701–12706 (2008).

[2] J. Yang *et al.*, "Imaging CF_3 I conical intersection and photodissociation dynamics with ultrafast electron diffraction," Science **361**, 64–67 (2018).

[3] T. R. Nelson *et al.*, "Non-adiabatic excited-state molecular dynamics: Theory and applications for modeling photophysics in extended molecular materials," Chem. Rev. **120**, 2215–2287 (2020).

[4] Y.-P. Chang *et al.*, "Electronic dynamics created at conical intersections and its dephasing in aqueous solution," Nat. Phys. **21**, 137–145 (2025).

[5] M. Allan and D. B. Popovic, "Vibronic coupling and selectivity of vibrational excitation in the negative ion resonances of ozone," Chem. Phys. Lett. **268**, 50–54 (1997).

[6] Y. R. Liu *et al.*, "Manipulating photodissociation dynamics via an embedding UV pulse," Commun. Phys. **8**, 331 (2025).

[7] Y. Chang *et al.*, "Vibrationally excited molecular hydrogen production from the water photochemistry," Nat. Commun. **12**, 6303 (2021).

[8] M. E. Jones, S. E. Barlow, G. B. Ellison, and E. E. Ferguson, "Reactions of C+, He+, and Ne+ with vibrationally excited H_2 and D_2," Chem. Phys. Lett. **130**, 218–223 (1986).

[9] A. Zanchet, M. V. J. AgúndezHerrero, A. Aguado, O. Roncero, and O. Roncero, "Sulfur chemistry in the interstellar medium: The effect of vibrational excitation of H_2 in the reaction $S^+ + H_2 \rightarrow SH^+ + H$," AJ **146**, 125 (2013).

[10] R. D. Beck *et al.*, "Vibrational mode-specific reaction of methane on a nickel surface," Science **302**, 98–100 (2003).

[11] R. R. Smith, D. R. Killelea, D. F. DelSesto, and A. L. Utz, "Preference for vibrational over translational energy in a gas-surface reaction," Science **304**, 992–995 (2004).

[12] K. M. Bal and E. C. Neyts, "Quantifying the impact of vibrational nonequilibrium in plasma catalysis: Insights from a molecular dynamics model of dissociative chemisorption," J. Phys. D: Appl. Phys. **54**, 394004 (2021).

[13] Z. Nagy *et al.*, "The chemistry of ions in the Orion Bar I. – CH^+, SH^+, and CF^+: The effect of high electron density and vibrationally excited H_2 in a warm PDR surface," A&A **550**, A96 (2013).

[14] P. Gnaciński, "Interstellar H_2 toward HD 147888," A&A **549**, A37 (2013).

[15] E. Roueff and F. Lique, "Molecular excitation in the interstellar medium: Recent advances in collisional, radiative, and chemical processes," Chem. Rev. **113**, 8906–8938 (2013).

[16] F. F. Crim, "Chemical dynamics of vibrationally excited molecules: Controlling reactions in gases and on surfaces," Proc. Natl. Acad. Sci. U.S.A. **105**, 12654–12661 (2008).

[17] K. Gope, N. Mason, E. Krishnakumar, and V. S. Prabhudesai, "DEA dynamics of chlorine dioxide probed by velocity slice imaging," Phys. Chem. Chem. Phys. **21**, 14023–14032 (2019).

[18] K. Gope, V. S. Prabhudesai, N. J. Mason, and E. Krishnakumar, "Dissociation dynamics of transient anion formed via electron attachment to sulfur dioxide," J. Chem. Phys. **147**, 054304 (2017).

[19] K. Gope, V. Tadsare, V. S. Prabhudesai, and E. Krishnakumar, "Production of electronically excited NO via DEA to NO_2," Eur. Phys. J. D **71**, 323 (2017).

[20] Y. Chang *et al.*, "Hydroxyl super rotors from vacuum ultraviolet photodissociation of water," Nat. Commun. **10**, 1250 (2019).

[21] K. Yuan *et al.*, "Nonadiabatic dissociation dynamics in H_2O: Competition between rotationally and nonrotationally mediated pathways," Proc. Natl. Acad. Sci. U.S.A. **105**, 19148–19153 (2008).

[22] S. A. Harich, X. Yang, X. Yang, and R. N. Dixon, "Extremely rotationally excited OH from water (HOD) photodissociation through conical intersection," Phys. Rev. Lett. **87**, 253201 (2001).

[23] H. Hou *et al.*, "Enhanced reactivity of highly vibrationally excited molecules on metal surfaces," Science **284**, 1647–1650 (1999).

[24] I. C. Walker, J. M. Gingell, N. J. Mason, and G. Marston, "Dissociative electron attachment (DEA) in ozone 0–10 eV," J. Phys. B: At. Mol. Opt. Phys. **29**, 4749–4759 (1996).

[25] B. B. Shen, Y. Benitez, K. G. Lunny, and R. E. Continetti, "Internal energy dependence of the photodissociation dynamics of O_3^- using cryogenic photoelectron-photofragment coincidence spectroscopy," J. Chem. Phys. **147**, 094307 (2017).

[26] R. L. Miller *et al.*, "The 'Ozone Deficit' problem: O_2 (X, $v \geq 26$) + $O(^3P)$ from 226-nm ozone photodissociation," Science **265**, 1831–1838 (1994).

[27] S. K. Pathak and N. J. Mason, "Our shrinking ozone layer: Global perspectives and remedial measures," Reson **7**, 71–80 (2002).

[28] D. Ehhalt, M. Prather, F. Dentener, R. Derwent, E. Dlugokencky *et al.*, "Atmospheric chemistry and greenhouse gases," in Climate Change 2001: The Scientific Basis, Intergovernmental Panel on Climate Change, 2001, https://hal.science/hal-03333922.

[29] P. S. Monks *et al.*, "Tropospheric ozone and its precursors from the urban to the global scale from air quality to short-lived climate forcer," Atmos. Chem. Phys. **15**, 8889–8973 (2015).

[30] M. Griggs, "Absorption coefficients of ozone in the ultraviolet and visible regions," J. Chem. Phys. **49**, 857–859 (1968).

[31] J. Brion, A. Chakir, D. Daumont, J. Malicet, and C. Parisse, "High-resolution laboratory absorption cross section of O_3. Temperature effect," Chem. Phys. Lett. **213**, 610–612 (1993).

[32] K. Yoshino, D. E. Freeman, J. R. Esmond, and W. H. Parkinson, "Absolute absorption cross-section measurements of ozone in the wavelength region 238–335 nm and the temperature dependence," Planet. Space Sci. **36**, 395–398 (1988).

[33] R. Ono, T. Nakamura, and X. Zhang, "Photofragmentation laser-induced fluorescence of ozone using narrowband and broadband KrF excimer lasers," J. Phys. D: Appl. Phys. **52**, 045201 (2019).

12 October 2026 11:14:18

Published under an exclusive license by AIP Publishing

[34]J. W. Robinson and J. Guagliardo, "Laser-induced infrared fluorescence of ozone. Application to remote sensing," Spectrosc. Lett. **6**, 271–289 (1973).
[35]K. Larsson *et al.*, "Instantaneous imaging of ozone in a gliding arc discharge using photofragmentation laser-induced fluorescence," J. Phys. D: Appl. Phys. **51**, 135203 (2018).
[36]A. Campargue, A. Barbe, M.-R. De Backer-Barilly, Vl. G. Tyuterev, and S. Kassi, "The near infrared spectrum of ozone by CW-cavity ring down spectroscopy between 5850 and 7000 cm^{-1}: New observations and exhaustive review," Phys. Chem. Chem. Phys. **10**, 2925 (2008).
[37]A. Barbe *et al.*, "CW-Cavity ring Down spectroscopy of the ozone molecule in the 5980–6220 cm^{-1} region," J. Mol. Spectrosc. **242**, 156–175 (2007).
[38]J. Zhang and Y. T. Lee, "Crossed molecular beam study of the reaction Cl + O_3," J. Phys. Chem. A **101**, 6485–6495 (1997).
[39]J. Zhang, T.-T. Miau, and Y. T. Lee, "Crossed molecular beam study of the reaction Br + O_3," J. Phys. Chem. A **101**, 6922–6930 (1997).
[40]C. C. Kahler, E. Ansell, C. M. Upshur, and W. H. Green, "A crossed molecular beam study of NO + O_3 → NO^*_2 + O_2: The effect of ozone rotational energy," J. Chem. Phys. **80**, 3644–3650 (1984).
[41]J. L. D. Pablos *et al.*, "Total and elastic electron scattering cross sections from ozone at intermediate and high energies," J. Phys. B: At. Mol. Opt. Phys. **35**, 865–874 (2002).
[42]K. N. Joshipura, B. K. Antony, and M. Vinodkumar, "Electron scattering and ionization of ozone, O_2 and O_4 molecules," J. Phys. B: At., Mol. Opt. Phys. **35**, 4211–4221 (2002).
[43]T. W. Shyn and C. J. Sweeney, "Angular distribution of electrons elastically scattered from ozone," Phys. Rev. A **47**, 2919–2921 (1993).
[44]M. Allan, N. J. Mason, and J. A. Davies, "Study of electronically excited states of ozone by electron-energy-loss spectroscopy," J. Chem. Phys. **105**, 5665–5671 (1996).
[45]J. D. Skalny, S. Matejcik, A. Kiendler, A. Stamatovic, and T. D. Märk, "Dissociative electron attachment to ozone using a high-resolution crossed beams technique," Chem. Phys. Lett. **255**, 112–118 (1996).
[46]G. Senn *et al.*, "Low energy dissociative electron attachment to ozone," Phys. Rev. Lett. **82**, 5028–5031 (1999).
[47]S. Matejcik *et al.*, "Low-energy electron attachment to mixed ozone/oxygen clusters," Chem. Phys. Lett. **261**, 437–442 (1996).
[48]C. Lifshitz, R. L. C. Wu, J. C. Haartz, and T. O. Tiernan, "Associative detachment reactions of negative ions with O_3," J. Chem. Phys. **67**, 2381–2382 (1977).
[49]J. A. Fedchak, B. L. Peko, and R. L. Champion, "Detachment and charge transfer for collisions of negative ions with ozone," J. Chem. Phys. **103**, 981–985 (1995).
[50]R. K. Curran, "Negative ion formation in ozone," J. Chem. Phys. **35**, 1849–1851 (1961).
[51]M. Allan *et al.*, "Resonances in collisions of low-energy electrons with ozone: Experimental elastic and vibrationally inelastic differential cross sections and dissociative attachment spectra," J. Phys. B: At. Mol. Opt. Phys. **29**, 4727–4747 (1996).
[52]M. Allan *et al.*, "Production of vibrationally autodetaching in low-energy electron impact on ozone," J. Phys. B: At. Mol. Opt. Phys. **29**, 3487–3495 (1996).
[53]S. A. Rangwala, S. V. K. Kumar, E. Krishnakumar, and N. J. Mason, "Cross sections for the dissociative electron attachment to ozone," J. Phys. B: At. Mol. Opt. Phys. **32**, 3795–3804 (1999).
[54]J. F. Hiller and M. L. Vestal, "Laser photodissociation of O_3^- by triple quadrupole mass spectrometry," J. Chem. Phys. **74**, 6096–6105 (1981).
[55]B. M. Nestmann, S. V. K. Kumar, and S. D. Peyerimhoff, "Contribution of Feshbach resonance to the 1.3 eV dissociative-electron-attachment cross section of ozone," Phys. Rev. A **71**, 012705 (2005).
[56]S. Solomon, "Stratospheric ozone depletion: A review of concepts and history," Rev. Geophys. **37**, 275–316, https://doi.org/10.1029/1999rg900008 (1999).
[57]H. E. Kessenich, A. Seppälä, and C. J. Rodger, "Potential drivers of the recent large Antarctic ozone holes," Nat. Commun. **14**, 7259 (2023).
[58]Q.-B. Lu, "Cosmic-ray-driven electron-induced reactions of halogenated molecules adsorbed on ice surfaces: Implications for atmospheric ozone depletion and global climate change," Phys. Rep. **487**, 141–167 (2010).
[59]Q.-B. Lu and T. E. Madey, "Mechanism for giant Cl^- and F^- enhancements in electron-induced dissociation of CF_2Cl_2 coadsorbed with water or ammonia ices," Surf. Sci. **451**, 238–243 (2000).
[60]Q.-B. Lu, "Formulation of the cosmic ray–driven electron-induced reaction mechanism for quantitative understanding of global ozone depletion," Proc. Natl. Acad. Sci. U.S.A. **120**, e2303048120 (2023).
[61]S. Matejcik *et al.*, "Electron attachment to molecules and clusters of atmospheric relevance: Oxygen and ozone," Plasma Sources Sci. Technol. **6**, 140–146 (1997).
[62]P. Cicman *et al.*, "Dissociative electron attachment to ozone at very low energies revisited," Int. J. Mass Spectrom. **260**, 85–87 (2007).
[63]N. J. Mason, "Electron scattering from ozone. What do we know?," Phys. Scr. **68**, C37–C43 (2003).
[64]P. Cicman, M. Francis, J. D. Skalný, and T. D. Märk, "The ion extraction efficiency in a crossed beams experiment using a trochoidal electron monochromator," Int. J. Mass Spectrom. **223–224**, 271–278 (2003).
[65]M. T. Lee, S. E. Michelin, T. Kroin, and L. E. Machado, "Elastic cross sections for electron-ozone collisions," J. Phys. B: At. Mol. Opt. Phys. **31**, 1781–1792 (1998).
[66]M. Tashiro, K. Morokuma, and J. Tennyson, "R-matrix calculation of electron collisions with electronically excited O_2 molecules," Phys. Rev. A **73**, 052707 (2006).
[67]M. Gupta and K. L. Baluja, "Electron collisions with an ozone molecule using the *R* -matrix method," J. Phys. B: At. Mol. Opt. Phys. **38**, 4057–4073 (2005).
[68]R. Curik, F. A. Gianturco, and N. Sanna, "Resonant features in low-energy electron scattering from ozone," J. Phys. B: At. Mol. Opt. Phys. **32**, 4567–4580 (1999).
[69]B. K. Sarpal, K. Pfingst, B. M. Nestmann, and S. D. Peyerimhoff, "Resonances in the integral elastic scattering cross section of ozone below 20 eV," Chem. Phys. Lett. **230**, 231–236 (1994).
[70]E. Krishnakumar, S. Denifl, I. Čadež, S. Markelj, and N. J. Mason, "Dissociative electron attachment cross sections for H_2 and D_2," Phys. Rev. Lett. **106**, 243201 (2011).
[71]E. Szymańska, V. S. Prabhudesai, N. J. Mason, and E. Krishnakumar, "Dissociative electron attachment to acetaldehyde, CH_3 CHO. A laboratory study using the velocity map imaging technique," Phys. Chem. Chem. Phys. **15**, 998–1005 (2013).
[72]K. Gope, V. S. Prabhudesai, N. J. Mason, and E. Krishnakumar, "Probing the resonant states of Cl_2 using velocity slice imaging," J. Phys. B: At. Mol. Opt. Phys. **49**, 015201 (2016).
[73]G. Horvath, J. D. Skalny, J. Orszagh, S. Matejcik, and N. J. Mason, "UV study of ozone decomposition on metal surfaces," in *WDS'07 Proceedings of Contributed Papers, Part II* (MatfyzPress, 2007), pp. 129–133, ISBN: 978-80-7378-024-1, https://www.mff.cuni.cz/veda/konference/wds/proc/pdf07/WDS07_219_f2_Horvath.pdf.
[74]B. Dhandapani and S. T. Oyama, "Gas phase ozone decomposition catalysts," Appl. Catal., B **11**, 129–166 (1997).
[75]D. Rapp and D. D. Briglia, "Total cross sections for ionization and attachment in gases by electron impact. II. Negative-ion formation," J. Chem. Phys. **43**, 1480–1489 (1965).
[76]J. D. Cox, D. D. Wagman, and V. A. Medvedev, *CODATA Key Values for Thermodynamics* (Hemisphere Publishing Corp. 1989), Vol. 1, https://www.codata.info/resources/databases/key1.html.
[77]M. W. Chase, "NIST-JANAF themochemical tables," J. Phys. Chem. Ref. Data, Monograph **9**, 1–1951 (1998), available at https://janaf.nist.gov/pdf/JANAF-FourthEd-1998-1Vol1-Intro.pdf.
[78]D. M. Neumark, K. R. Lykke, T. Andersen, and W. C. Lineberger, "Laser photodetachment measurement of the electron affinity of atomic oxygen," Phys. Rev. A **32**, 1890–1892 (1985).
[79]R. J. Celotta, R. A. Bennett, J. L. Hall, M. W. Siegel, and J. Levine, "Molecular photodetachment spectrometry. II. The electron affinity of O_2 and the structure of O_2," Phys. Rev. A **6**, 631–642 (1972).

12 October 2026 11:14:18

Published under an exclusive license by AIP Publishing

[80]D. W. Arnold, C. Xu, E. H. Kim, and D. M. Neumark, "Study of low-lying electronic states of ozone by anion photoelectron spectroscopy of O_3^-," J. Chem. Phys. **101**, 912–922 (1994).
[81]K. A. Peterson, R. C. Mayrhofer, and R. C. Woods, "The potential energy and dipole moment surfaces of NF_2 and O_3^- by complete active space self-consistent field," J. Chem. Phys. **93**, 5020–5028 (1990).
[82]A. Moradmand, D. S. Slaughter, A. L. Landers, and M. Fogle, "Dissociative-electron-attachment dynamics near the 8-eV Feshbach resonance of CO_2," Phys. Rev. A **88**, 022711 (2013).
[83]W. Koch *et al.*, "The low lying electronic states of O_3^-," J. Chem. Phys. **99**, 1271–1277 (1993).
[84]P. Wang, S. Gong, and Y. Mo, "Bond dissociation energy of O_2 measured by fully state-to-state resolved threshold fragment yield spectra," J. Chem. Phys. **160**, 164302 (2024).
[85]T. F. O'Malley and H. S. Taylor, "Angular dependence of scattering products in electron-molecule resonant excitation and in dissociative attachment," Phys. Rev. **176**, 207–221 (1968).
[86]R. Azria, Y. L. Coat, G. Lefevre, and D. Simon, "Dissociative electron attachment on H_2S: Energy and angular distributions of H^- ions," J. Phys. B: At. Mol. Phys. **12**, 679–687 (1979).
[87]N. B. Ram, V. S. Prabhudesai, and E. Krishnakumar, "Comment on "Imaging the molecular dynamics of dissociative electron attachment to water"," Phys. Rev. Lett. **106**, 049301 (2011).

12 October 2026 11:14:18

Published under an exclusive license by AIP Publishing